PHYSICAL REVIEW C **108**, 014605 (2023)

Light projectile elastic scattering by nuclei described by the Gogny interaction

J. López Moraña[1] and X. Viñas [1,2]

[1]*Departament de Física Quàntica i Astrofísica (FQA) and Institut de Ciències del Cosmos (ICCUB),*
Universitat de Barcelona (UB), Martí i Franquès 1, E-08028 Barcelona, Spain
[2]*Institut Menorquí d'Estudis, Camí des Castell 28, 07702 Maó, Spain*

(Received 23 April 2023; revised 11 June 2023; accepted 28 June 2023; published 17 July 2023)

In this work, we study the elastic scattering of some light particles, such as ^{2}H, ^{3}H, ^{3}He, and ^{4}He, by heavy target nuclei with an extended Watanabe model, which uses as input the neutron-nucleus and proton-nucleus optical potentials and the ground-state wave functions of the projectile. The nucleon-nucleus optical potential used in this work was obtained within a semimicroscopic nuclear matter approach, whose real and imaginary parts are provided by the first- and second-order terms, respectively, of the Taylor expansion of the Brueckner-Hartree-Fock mass operator obtained with the reaction G matrix built up with the Gogny force [J. Lopez Moraña and X. Viñas, J. Phys. G **48**, 035104 (2021)]. The angular distributions of the scattering of ^{2}H, ^{3}H, ^{3}He, and ^{4}He from different target nuclei and at different incident energies of the projectile computed with this model are analyzed. The reaction cross sections corresponding to some of these scattering processes are also calculated. Our results are compared with the experimental values as well as with another Watanabe calculation where the nucleon-nucleus optical potential is provided by the phenomenological Köning-Delaroche model. The limitations of the extended Watanabe model used in this work are also discussed.

DOI: 10.1103/PhysRevC.108.014605

I. INTRODUCTION

The theoretical analysis of the scattering of nucleons by nuclei is usually performed with the help of the optical model [1], which allows one to predict different observables such as the elastic scattering angular distributions, the total reaction cross sections, and the analyzing powers in a relatively simple way. The optical potential can be built up in two different manners. In the case of phenomenological optical potentials, one assumes some analytical profile for the radial dependence of the potential, usually of Woods-Saxon type, and fits their parameters to reproduce a selected set of measurements of different scattering observables in some particular reactions [2–4]. The optical potential can also be determined from more microscopic grounds, which often are based on the fact that this potential could be identified with the mass operator of the one-particle Green function [5]. Following this idea, Jeukene, Lejeune, and Mahaux derived a microscopic optical potential performing Brueckner-Hartree-Fock (BHF) calculations in nuclear matter using realistic nucleon-nucleon interactions. This microscopic optical potential was applied to finite nuclei using the local density approximation (LDA) with parametrized nuclear densities [6–10]. However, effective forces such as the Skyrme [11] or Gogny [12] interactions, which are specially designed to describe ground-state properties of finite nuclei, have also been used to obtain a nucleon-nucleus microscopic optical potential [13–18]. The underlying idea, in this case, is that these forces can be regarded as effective parametrization of the G matrix and used to obtain perturbatively the first- and second-order terms of the expansion of the mass operator of the one-body Green function.

A different approximation to obtain the microscopic optical potential is the folding model [19,20], where the optical potential is computed by convolution of a complex two-body nucleon-nucleon effective interaction [21–27] with the target nucleus density. It can be seen from basic folding formulas that the method generates the first-order term of the microscopic optical potential derived from Feshbach's theory [28]. This model is used quite often as a basis to describe the scattering of light projectiles by heavier nuclei. In this case, the corresponding microscopic optical potential can be obtained by folding the projectile density with the nucleon-nucleus optical potential, which represents the interaction of a free nucleon of the projectile with the target nucleus [29–33].

In a previous paper [18] we developed a microscopic model to describe nucleon-nucleus scattering at relatively low bombarding energy using Gogny forces of the D1 family. The real and imaginary parts of this microscopic optical potential are obtained as the first- and second-order terms of the Taylor expansion of the mass operator, respectively, which are calculated within the BHF method using the G-matrix built up with the effective Gogny force. This optical potential is applied to finite nuclei using the LDA with the neutron and proton densities computed within a quasilocal Hartree-Fock approximation with the same Gogny interaction [34,35]. This nucleon-nucleus microscopic optical potential [18] does not contain free parameters to be adjusted to scattering data and gives a reasonably good agreement with the experimental results of differential cross sections and analyzing powers of neutron and proton elastic scattering by atomic nuclei along the whole periodic table. Very recently, this model was used successfully to describe quasielastic proton-neutron charge exchange reactions [36].

We want to continue analyzing the ability of this Gogny-based microscopic optical potential to describe other scattering processes. In particular, in this work, we perform an exploratory study of the elastic scattering of light projectiles ^{2}H, ^{3}H, ^{3}He, and ^{4}He by atomic nuclei through a relatively simple folding model. Actually, we follow a strategy similar to that used in Refs. [37–43] for describing this type of reaction with a microscopic optical potential built up with effective Skyrme forces. We are aware that this simple model corresponds to the free scattering of the nucleon of the projectile by the target nucleus disregarding other possible reaction channels, such as inelastic scattering and breakup and transfer reactions, which are taken into account, on average, in the imaginary part of the optical potential. Thus the microscopic optical potential used in this work becomes an extended Watanabe model [44] for describing the light-particle–nucleus elastic scattering (the original Watanabe model takes into account only deuteron-nucleus elastic scattering). In order to account for the breakup effects, the more fundamental continuum discretized coupled-channels (CDCC) method was introduced long ago by Rawitscher [45]. More recently, Mackintosh and Keeley pointed out the relevance of the pickup reactions in the coupled-channels calculations for a precise description of the ^{2}He-nucleus [46], ^{3}He-nucleus [47], and ^{3}H-nucleus [48,49] elastic scatterings. In order to check the reliability of our model, we have compared our results for some deuteron-induced reactions with the CDCC results reported in Ref. [50], using in both cases the phenomenonogical optical potential of Köning-Delaroche as underlying nucleon-nucleus optical potential. Also we have estimated the impact of including the pickup channels on the elastic scattering calculation for two reactions by comparing our results with the predictions of the coupled reaction channel (CRC) calculations of Ref. [46,48].

The paper is organized as follows. In Sec. II we summarize our theory. Section III is devoted to discussing the predictions of our model concerning several elastic scattering observables measured in different reactions induced by ^{2}H, ^{3}H, ^{3}He, and ^{4}He. Our conclusions are laid out in the last section. The Appendix summarizes the renormalization procedure of the Gogny-based nucleon-nucleus optical potentials.

II. BASIC THEORY

To describe elastic scattering by light particles we use an extended version of the Watanabe model [44], which was initially devised for describing high energy scattering of deuterons by complex nuclei.

A. The Watanabe model

In this model, it is assumed that the scattering of deuterons by heavier nuclei is described by the wave function solution of the following Schrödinger equation:

$$\left\{-\frac{\hbar^2}{2M}\nabla_{\mathbf{R}}{}^2-\frac{\hbar^2}{2\mu}\nabla_{\mathbf{s}}{}^2+V_{12}(\mathbf{s})+V_1\left(\mathbf{R}+\frac{\mathbf{s}}{2}\right)+V_2\left(\mathbf{R}-\frac{\mathbf{s}}{2}\right)\right\}\Psi(\mathbf{R},\mathbf{s})=E\Psi(\mathbf{R},\mathbf{s}), \tag{1}$$

which is written in terms of the neutron and proton center of mass and relative coordinates, $\mathbf{R}=(\mathbf{r}_1+\mathbf{r}_1)/2$ and $\mathbf{s}=\mathbf{r}_1-\mathbf{r}_2$. In this equation $M=m_n+m_p$ and $\mu=m_nm_p/(m_n+m_p)$ are the total and reduced masses of the two nucleons, V_1 and V_2 represents the interaction of the neutron and proton with the target nucleus, and V_{12} is the neutron-proton interaction in the deuteron.

The wave function solution of the Schrödinger equation (1) can be written as [44]

$$\Psi(\mathbf{R},\mathbf{s})=\chi_0(\mathbf{s})\Phi(\mathbf{R})+F(\mathbf{R},\mathbf{s}), \tag{2}$$

where $\chi_0(\mathbf{s})$ is the ground state-deuteron wave function, $\Phi(\mathbf{R})$ describes the center-of-mass motion and $F(\mathbf{R},\mathbf{s})$ takes into account the coupling between the center of mass and the relative motion.

The ground-state deuteron wave function, which corresponds to total spin and isospin $S=1$ and $T=0$, respectively, does not contain D-wave admixture and is the solution of the intrinsic Schrödinger equation

$$\left\{-\frac{\hbar^2}{2\mu}\nabla_{\mathbf{s}}{}^2+V_{12}(\mathbf{s})\right\}\chi_0=\epsilon_d\chi_0, \tag{3}$$

which together with the wave functions $\chi_i(i=1,2,\dots)$, also solutions of the equation $H_{in}\chi_i=\epsilon_i\chi_i$ and orthogonal to χ_0, form a complete set of wave functions, which, assuming a discretized continuum, allows one to write [37,50]

$$F(\mathbf{R},\mathbf{s})=\sum_{i>0}\chi_i(\mathbf{s})\phi_i(\mathbf{R}). \tag{4}$$

Next, multiplying the Schrödinger equation (1) by $\chi_0^\dagger$ and integrating over the relative coordinate, one obtains

$$-\frac{\hbar^2}{2M}\nabla_{\mathbf{R}}{}^2\Phi(\mathbf{R})+V(\mathbf{R})\Phi(\mathbf{R})+g(\mathbf{R})=(E-\epsilon_d)\Phi(\mathbf{R}), \tag{5}$$

where

$$V(\mathbf{R})=\int d\mathbf{s}\chi_0^\dagger(\mathbf{s})\left[V_1\left(\mathbf{R}+\frac{\mathbf{s}}{2}\right)+V_2\left(\mathbf{R}-\frac{\mathbf{s}}{2}\right)\right]\chi_0(\mathbf{s}) \tag{6}$$

and

$$g(\mathbf{R})=\int d\mathbf{s}\chi_0^\dagger(\mathbf{s})\left[V_1\left(\mathbf{R}+\frac{\mathbf{s}}{2}\right)+V_2\left(\mathbf{R}-\frac{\mathbf{s}}{2}\right)\right]F(\mathbf{R},\mathbf{s}). \tag{7}$$

The last contribution in the left-hand side of (5), $g(\mathbf{R})$, contains the breakup of the deuteron and the distortion of the deuteron wave function. These effects in the simplest version of the Watanabe model are approximated by adding an imaginary contribution to $V(\mathbf{R})$ and dropping $g(\mathbf{R})$. In a last step, the potentials V_1 and V_2 in (7) are replaced by the corresponding neutron-nucleus and proton-nucleus optical potentials. The dipole polarizability in the deuteron scattering is a manifestation of the coupling to breakup channels via the electric dipole operator [51]. This effect has an important effect on energies around the Coulomb barrier [52]. It was pointed out some time ago that the trivially local equivalent polarization potential describing the effect of the breakup channels on elastic scattering has both real and imaginary contributions [53]. Although the breakup effects and the impact of the dipole polarizability have not been included explicitly in our model, we expect they are included, at least partially, in an effective way through the imaginary part of the optical potential, as in the original Watanabe work [44]. We have checked our approach by performing some comparisons between the differential and total cross sections computed with the original Watanabe model and the CDCC results of Ref. [50].

B. The extended Watanabe model

In order to describe the elastic scattering of ^{3}H, ^{3}He, and ^{4}He by heavier nuclei, we use a generalized Watanabe model where the microscopic projectile-target optical potential is obtained by folding the nucleon-target optical potential of the constituents nucleons in the ground state of the projectile. It can be written as

$$V(\mathbf{R}) = \sum_{i=1}^{n} \langle \chi_0(\xi_1,\dots,\xi_{n-1}) | V_i \times (\mathbf{R},\xi_1,\dots,\xi_{n-1}) | \chi_0(\xi_1,\dots,\xi_{n-1}) \rangle, \tag{8}$$

where n is the number of nucleons in the projectile, $V_i(\mathbf{R},\xi_1,\dots,\xi_{n-1})$ is the free nucleon-target optical potential corresponding to the nucleon i, and $\chi_0(\xi_1,\dots,\xi_{n-1})$ is the ground-state wave function of the projectile, both written in terms of the Jacobi coordinates. In this system $\mathbf{R}$ is the center-of-mass position of the projectile and ξ_i $(i = 1,\dots,n-1)$ are the relative coordinates related to the positions $\mathbf{r}_1, \mathbf{r}_2, \dots, \mathbf{r}_n$ of each nucleon in the projectile:

$$\mathbf{R} = \frac{1}{n}\sum_{i=1}^{n} \mathbf{r}_i,$$

$$\xi_j = \frac{1}{j}\sum_{k=1}^{j} \mathbf{r}_k - \mathbf{r}_{j+1} \quad (j = 1, 2, \dots, n-1), \tag{9}$$

where $n = 2$ for ^{2}H, $n = 3$ for ^{3}H, and ^{3}He and $n = 4$ for ^{4}He.

The wave functions of the different projectiles, which enter in (8), are expressed in terms of the intrinsic coordinates. In the case of the deuteron the ground-state wave function, assuming only s-wave contribution, is expressed by the Hulthén function [39]

$$\Phi_{^2H}(\xi_1) = \frac{N_d}{\xi_1}[e^{-\alpha\xi_1} - e^{-\beta\xi_1}], \tag{10}$$

where $N_d = \sqrt{\frac{\alpha\beta(\alpha+\beta)}{2\pi(\beta-\alpha)^2}}$ with $\alpha = 0.23$ fm^{-1} and $\beta = 1.61$ fm^{-1}.

For ^{3}H and ^{3}He the spatial part of the intrinsic wave functions are expressed by the three-dimensional harmonic oscillator functions as [40,41]

$$\Phi_{^3H}(\xi_1,\xi_2) = \Phi_{^3He}(\xi_1,\xi_2) = \left(\frac{\beta^2}{3\pi^2}\right)^{\frac{3}{4}} e^{-\frac{\beta\xi_1^2}{4} - \frac{\beta\xi_2^2}{3}}, \tag{11}$$

where $\beta = 0.346$ fm^{-2} for ^{3}H and $\beta = 0.283$ fm^{-2} for ^{3}He. Notice that the full wave functions of these two nuclei also contain, in addition to the spatial part, spin and isospin contributions. In order to preserve the antisymmetry, the two identical particles are coupled to isospin $T = 1$ and spin $S = 0$. When the third nucleon is added, the total spin and isospin become $S_t = 1/2$ and $T_t = 1/2$, because the ground states of ^{3}H and ^{3}He are a isospin doublet. These total spin and isospin values together with the symmetric spatial part of the wave functions of these nuclei given by Eq. (11) implies that in their ground state they have spin-parity $J^\pi = 1/2^+$, which is in agreement with the experimental values. However, as far as the optical potential (8) only depends on spatial variables, the spin and isospin structure of the ^{3}H and ^{3}He do not play any role in its calculation.

Again using harmonic oscillator wave functions the wave function of ^{4}He can be written as

$$\Phi_{^4He}(\xi_1,\xi_2,\xi_3) = \left(\frac{\beta^3}{4\pi^3}\right)^{\frac{3}{4}} e^{-\frac{\beta(\xi_1^2+\xi_2^2)}{4} - \frac{\beta\xi_3^2}{2}}, \tag{12}$$

where in this case $\beta = 0.4395$ fm^{-2} [42].

C. The nucleon-nucleus optical potential

The other piece of the Watanabe model is the free nucleon-nucleus optical potential, which we have derived in a previous publication [18] on the basis of a semi-microscopic nuclear matter approximation using Gogny forces of the D1 family. Gogny interactions were introduced by Gogny in the early 1980s [12], aimed to describe simultaneously the mean field and the pairing field of finite nuclei with the same interaction. The Gogny D1S parametrization [54] has been used in large-scale Hartree-Fock-Bogoliubov calculations of ground-state properties of finite nuclei along the whole periodic table [55]. A detailed analysis of these results shows some deficiencies in the theoretical description of masses of neutron-rich nuclei compared with the corresponding experimental values (see [56] for more details). To remedy these limitations of D1S, new parametrizations of the Gogny force, namely D1N [57] and D1M [58], have been proposed. These forces incorporate in their fitting protocol the constraint of reproducing, in a qualitative way, the microscopic equation of state of Friedman and Pandharipande in neutron matter in order to improve the description of neutron-rich nuclei.

The Gogny forces of the D1 family consist of a finite-range part and a zero-range density-dependent term together with spin-orbit interaction, which is also zero range as in the case of Skyrme forces. The finite-range part is the sum of two Gaussian form factors with different ranges, each multiplied by all the possible spin-isospin exchange operators with different weights. Therefore this type of Gogny force reads

$$\begin{aligned} V(\vec{r}_{12}) = {} & t_3(1+\hat{P}_\sigma)\delta(\vec{r}_{12})\left[\rho\left(\frac{\vec{r}_1+\vec{r}_2}{2}\right)\right]^{1/3} + \sum_{k=1}^{k=2} e^{-\left(\frac{\vec{r}_{12}}{\mu_k}\right)^2} \\ & \times (W_k + B_k\hat{P}_\sigma - H_k\hat{P}_\tau - M_k\hat{P}_\sigma\hat{P}_\tau) \\ & + iW_{LS}(\hat{\sigma}_1+\hat{\sigma}_2)\cdot\hat{k}^\dagger \times \delta(\vec{r}_{12})\hat{k}, \end{aligned} \tag{13}$$

where

$$\hat{P}_\sigma = \tfrac{1}{2}(1+\hat{\sigma}_1\cdot\hat{\sigma}_2) \quad \text{and} \quad \hat{P}_\tau = \tfrac{1}{2}(1+\hat{\tau}_1\cdot\hat{\tau}_2)$$

are the spin and isospin exchange operators, respectively, while

$$\vec{r}_{12} = \vec{r}_1 - \vec{r}_2 \quad \text{and} \quad \hat{k} = \frac{1}{2i}(\vec{\nabla}_1 - \vec{\nabla}_2)$$

TABLE I. Parameters of the effective D1S Gogny force used in this work.

	k	μ_k (fm)	W_k	B_k	H_k	M_k (MeV)
D1S	1	0.7	−1720.3	1300	−1813.53	1397.60
	2	1.2	103.64	−163.48	162.81	−223.93
D1S	$W_{LS} = 130$ MeV fm^5			$t_3 = 1390$ MeV fm^4		

are the relative coordinate and the relative momentum of the two nucleons, respectively. The parameters of the force, namely $W_k, B_k, H_k, M_k, \mu_k$ $(k = 1, 2)$, t_3, and W_{LS} are fitted to reproduce some properties of finite nuclei and infinite nuclear matter (see Refs. [12] and [58] for more details about the fitting protocol of Gogny interactions).

Let us summarize the more relevant aspects of the microscopic optical potential based on the Gogny interaction, which was derived in Ref. [18] and will be used in the present work. It is obtained with the Jeukene, Lejeune, and Mahaux procedure [6–9] in nuclear matter. The real and imaginary parts of the central potential are determined from the first and second terms of the Taylor expansion of the mass operator, which is computed using the effective Gogny force instead of a microscopic interaction. In the present work, we use the D1S parametrization of the Gogny force, whose parameters are given in Table I. In Ref. [18] we checked that the use of other parametrizations of the Gogny force such as D1N or D1M provides basically the same description of the nucleon-nucleus elastic scattering. The model described here based on the Gogny interaction is similar to other microscopic optical potentials obtained from the same theoretical grounds but using Skyrme forces [13–17].

In this model, the real part of the central potential corresponds to the single-particle potential felt by the incident projectile due to the nucleon in the target. In the strict application of the model, this real part is the Hartree-Fock (HF) single-particle potential in nuclear matter considering only the two-body part of the nucleon-nucleon interaction, which for an incident nucleon α of type τ reads

$$V_{\tau\alpha} = \frac{3}{2} t_3 \rho^{1/3}[\rho - \rho_{\tau\alpha}] + \pi^{3/2} \sum_{k=1}^{k=2} \mu_k^3 \left[\left(W_k + \frac{B_k}{2}\right)\rho - \left(H_k + \frac{M_k}{2}\right)\rho_{\tau\alpha}\right]$$
$$- \frac{1}{4\pi^{3/2}} \sum_{k=1}^{k=2} \mu_k^3 \left[\left(\frac{W_k}{2} + B_k - \frac{H_k}{2} - M_k\right) I(k_\alpha, k_\rho = k_{\tau\alpha}) - \left(\frac{H_k}{2} + M_k\right) I(k_\alpha, k_\rho = k_{-\tau\alpha})\right], \quad (14)$$

where the Fermi momenta of the particles with the same (opposite) isospin as the projectile are related to the corresponding particle densities by $k_{\tau\alpha}^3 = 3\pi^2\rho_{\tau\alpha}$ $(k_{-\tau\alpha}^3 = 3\pi^2\rho_{-\tau\alpha})$. In Eq. (14) the functions I, which depend on the momentum k_α of the projectile and correspond to the HF exchange potential, are defined as

$$I(k_\alpha, k_\rho) = \frac{4\pi^{3/2}}{\mu_k^3}\left[\operatorname{erf}\left(\frac{\mu_k}{2}(k_\rho - k_\alpha)\right) + \operatorname{erf}\left(\frac{\mu_k}{2}(k_\rho + k_\alpha)\right)\right] + \frac{8\pi}{k_\alpha \mu_k^4}\left[e^{-\frac{\mu_k^2}{4}(k_\alpha + k_\rho)^2} - e^{-\frac{\mu_k^2}{4}(k_\alpha - k_\rho)^2}\right]. \quad (15)$$

To obtain the real part of the central potential in a finite nucleus we apply the LDA in (14) with the self-consistent neutron and proton densities of the target computed within the quasilocal density formalism [18,34,35], which allows one to express $V_{\tau\alpha}$ as a function of the position through the densities and local Fermi momenta of neutrons and protons in Eq. (14). The radial dependence of the momentum of the incident neutron k_α is given by the solution of the equation

$$E_L = \frac{\hbar^2 k_\alpha^2}{2m} + V_{\tau\alpha}(k_\alpha, k_{\tau\alpha}(R), k_{-\tau\alpha}(R)), \quad (16)$$

where E_L is the energy of the projectile in the laboratory frame [if the projectile is a proton the Coulomb potential of the target has to be added to (16)]. Due to the finite range of the Gogny force the momentum of the incident nucleon k_α appears in the kinetic and potential contributions to Eq. (16), which implies that this equation has not an exact analytical solution and therefore the momentum k_α must be obtained numerically. However, the momentum of the incident nucleon can still be obtained approximately in an analytical way by performing locally a quadratic Taylor expansion of $V_{\tau\alpha}$ around the Fermi momentum $k_{\tau\alpha}$ of the particles with the same isospin as the projectile, i.e.,

$$V_{\tau\alpha}(R) = V_{\tau\alpha}(k_\alpha = k_{\tau\alpha}, R) + \left[\frac{1}{2k_\alpha}\frac{\partial V_{\tau\alpha}(k_\alpha, R)}{\partial k_\alpha}\right]_{k_\alpha = k_{\tau\alpha}} (k_\alpha^2 - k_{\tau\alpha}^2), \quad (17)$$

where the coordinate R indicates the radial dependence of the real part of the central potential, owing to its dependence on the local neutron and proton Fermi momenta of the target. With this approximation Eq. (16) can be recast as

$$E_L = \frac{\hbar^2 k_\alpha^2}{2m_{\tau\alpha}^*} + V_{0\tau\alpha}(R), \quad (18)$$

where $m_{\tau\alpha}^*$ is the effective mass at the Fermi momentum $k_{\tau\alpha}$, defined as

$$\frac{m}{m_{\tau\alpha}^*} = 1 + \frac{m}{\hbar^2}\frac{1}{k_{\tau\alpha}}\left[\frac{\partial V_{\tau\alpha}}{\partial k_\alpha}\right]_{k_\alpha = k_{\tau\alpha}}, \quad (19)$$

and

$$V_{0\tau\alpha} = V_{\tau\alpha}(k_\alpha = k_{\tau\alpha}) - \frac{k_{\tau\alpha}}{2}\left[\frac{\partial V_{\tau\alpha}}{\partial k_\alpha}.\right]_{k_\alpha = k_{\tau\alpha}} \quad (20)$$

The imaginary part of the central potential is given by [18]

$$W_\alpha = \frac{1}{2} Im \sum_{\substack{\nu \leqslant k_F \\ \lambda,\mu > k_F}} \langle \alpha\nu|V|\widetilde{\lambda\mu}\rangle \frac{1}{\epsilon_\alpha + \epsilon_\nu - \epsilon_\lambda - \epsilon_\mu + i\eta} \times \langle \lambda\mu|V|\widetilde{\alpha\nu}\rangle. \tag{21}$$

The denominator of this expression can be easily worked out by making use of the parabolic approach, which allows writing the single-particle energy of the projectile as (18) and similar expressions for the other particle and hole states entering in Eq. (21). Due to the charge conservation, we can write the denominator of (21) as

$$\varepsilon_\alpha + \varepsilon_\nu - \varepsilon_\lambda - \varepsilon_\mu = \frac{\hbar^2 k_\alpha^2}{2m^*_{\tau\alpha}} + \frac{\hbar^2 k_\nu^2}{2m^*_{\tau\nu}} - \frac{\hbar^2 k_\lambda^2}{2m^*_{\tau\lambda}} - \frac{\hbar^2 k_\mu^2}{2m^*_{\tau\mu}}. \tag{22}$$

Applying the principal value integral to deal with the denominator of (21), after some lengthy algebra one obtains the imaginary part of the central potential in the nuclear matter approach, which can be finally expressed as

$$W_{\tau\alpha} = -\frac{1}{2}\frac{\pi}{(2\pi)^6}[W_1 + 2W_2 + W_3 + W_4 + W_5], \tag{23}$$

where the different contributions to (23) are given in [18].

The microscopic nucleon-nucleus optical potential that describes the light-particle target scattering (8) also contains Coulomb and spin-orbit contributions. The Coulomb potential in the light-particle microscopic optical potential is included in the different proton-nucleus potentials entering in Eq. (8). Except in the case of ^{4}He where it vanishes, the spin-orbit potentials in the other light particles considered in this work are consistent with the sum of the spin-orbit potentials for their constituent nucleons. Notice, however, that the spin-orbit for the deuteron is multiplied by an energy factor [39], which takes into account the energy dependence of the spin-orbit potential in this case, and for tritium the spin-orbit energy of each constituent is multiplied by the corresponding effective mass in order to enhance the spin-orbit contribution at the nuclear surface [40]. Note that, in the calculations reported in the next section, we have replaced the real part of the single-particle potential in the nuclear matter approach with the one obtained in the HF approximation, which takes into account the finite size of the target nucleus as well as the rearrangement contributions (see [18] for more details).

III. RESULTS

A. Optical potentials for the scattering of light projectiles from nuclei

As we have discussed previously, the microscopic optical potential for describing the elastic scattering of deuterons from nuclei used in this work is built up with the help of the Watanabe model and is given by Eq. (6), where V_1 and V_2 are the neutron-nucleus and proton-nucleus microscopical optical potentials based on the Gogny D1S effective force and derived in Ref. [18].

Using the optical potential provided by the extended Watanabe model (8) with the intrinsic wave functions for ^{3}H, ^{3}He, and ^{4}He given by Eqs. (11) and (12), the microscopic optical potential for describing ^{3}H and ^{3}He scattering from heavier nuclei reads

$$V_{^3\mathrm{H}(^3\mathrm{He})}(\mathbf{R}) = \int d\xi_1 d\xi_2 \chi_0^\dagger(\xi_1,\xi_2)\left[V_{n(p)}\left(\mathbf{R} + \frac{\xi_1}{2} + \frac{\xi_2}{3}\right) + V_{n(p)}\left(\mathbf{R} - \frac{\xi_1}{2} + \frac{\xi_2}{3}\right) + V_{p(n)}\left(\mathbf{R} - \frac{2\xi_2}{3}\right)\right]\chi_0(\xi_1,\xi_2), \tag{24}$$

and for scattering of α particles is given by

$$V_{^4\mathrm{He}}(\mathbf{R}) = \int d\xi_1 d\xi_2 d\xi_3 \chi_0^\dagger(\xi_1,\xi_2,\xi_3)\left[V_n\left(\mathbf{R} + \frac{\xi_1}{2} + \frac{\xi_3}{2}\right) + V_n\left(\mathbf{R} - \frac{\xi_1}{2} + \frac{\xi_3}{2}\right) + V_p\left(\mathbf{R} + \frac{\xi_2}{2} - \frac{\xi_3}{2}\right) + V_p\left(\mathbf{R} - \frac{\xi_2}{2} - \frac{\xi_3}{2}\right)\right]\chi_0(\xi_1,\xi_2,\xi_2), \tag{25}$$

where V_n and V_p are the neutron-nucleus and proton-nucleus optical potentials obtained as explained in Sec. II C. At this point, two comments are in order. First, within the theoretical model used in this work, the energy E of the projectile is shared among its nucleons, which means that the neutron-nucleus and proton-nucleus optical potentials entering in Eqs. (6), (24), and (25) are computed at energy values of $E/2$, $E/3$, and $E/4$, respectively. Second, if this energy is smaller than the Coulomb barrier of the proton-target system, the real and imaginary parts of the central potential are not taken into account and the proton-nucleus optical potential reduces to its Coulomb contribution. However, this prescription may be an oversimplification that underestimates the reaction cross section because, as explained in Ref. [59], in the scattering of a composite weakly bound particle, such as ^{2}H, ^{3}H, or ^{3}He, there is a reaction probability even in the case that the energy of a fragment is below that of the fragment-target Coulomb barrier due to the Trojan horse effect [60].

The real and imaginary parts of the central contribution to the microscopic optical potential based on the Gogny force for describing the elastic scattering of light particles from heavier targets (MOPG hereafter), show, as a function of the energy of the incident projectile, some global trends that are largely independent of the projectile and of the target nucleus. Just as an example, we show in the different panels of Fig. 1 the evolution with the energy of the projectile of the profiles of real and imaginary parts of the central term of the MOPG provided by Eqs. (6) and (25) for the reactions ^{2}H-^{208}Pb and ^{4}He-^{208}Pb. From this figure, we can see that in all the cases the depth of the real part decreases with increasing energy, which points out the repulsive character of the energy dependence of the real part of the MOPG. However, the opposite trend happens

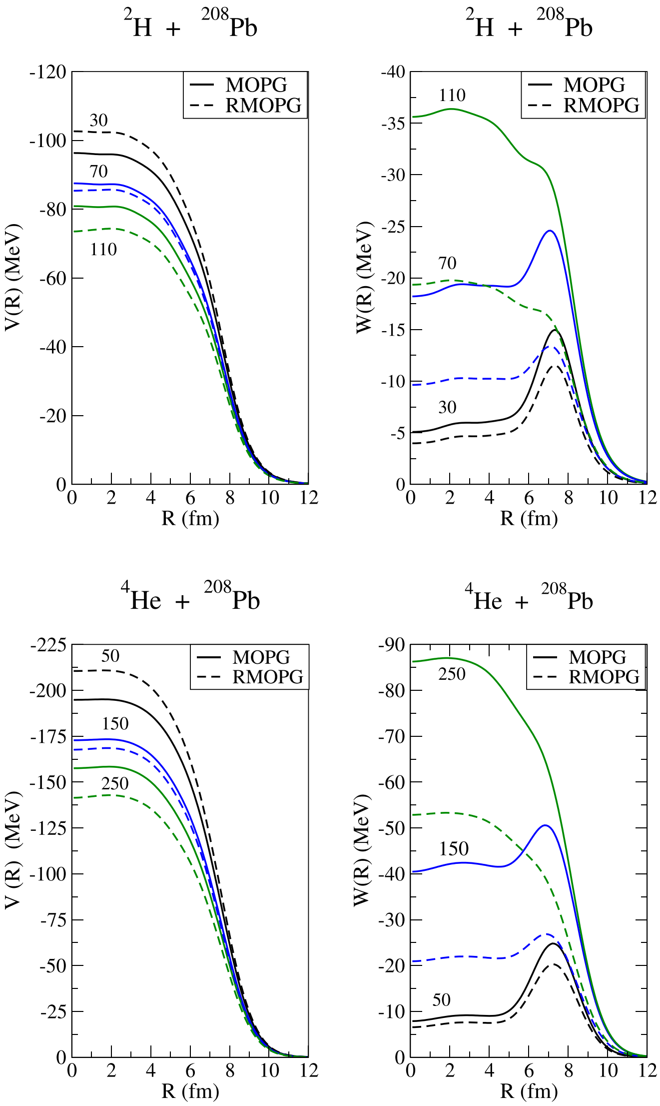

FIG. 1. Real and imaginary parts of the ^{2}H-^{208}Pb (up) and ^{4}He-^{208}Pb (down) microscopic optical potentials computed with our microscopic unrenormalized (MOPG) and renormalized (RMOPG) models at several energies of the projectile.

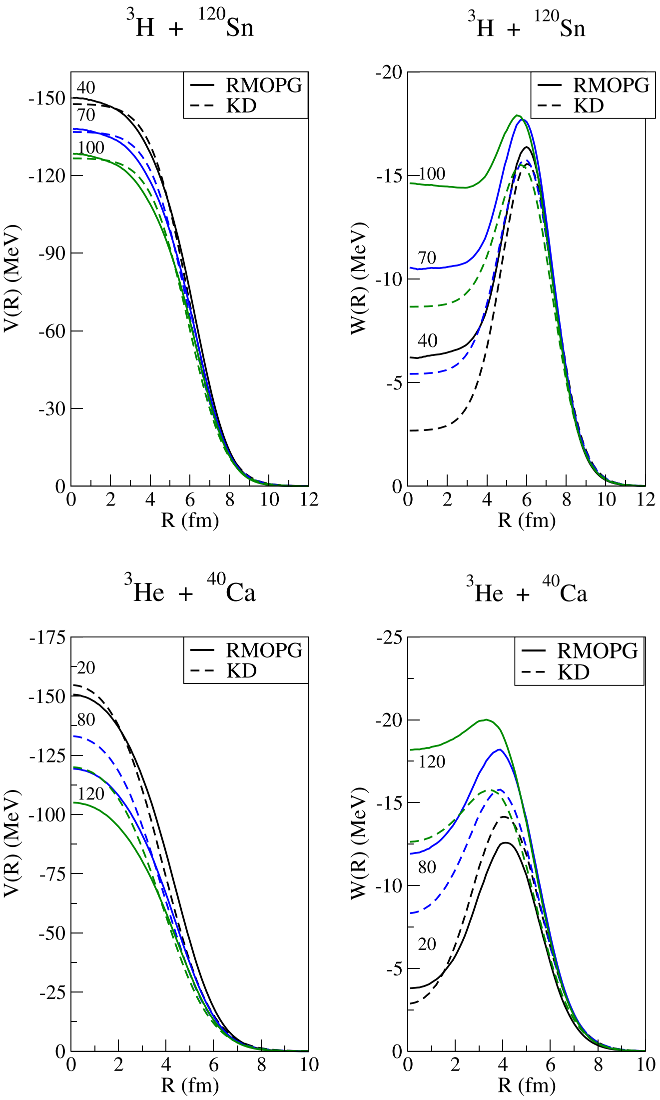

FIG. 2. Real and imaginary parts of ^{3}H-^{120}Sn (up) and ^{3}He-^{40}Ca (down) microscopic optical potentials computed with our renormalized model (RMOPG) and with a Watanabe model based on the Köning-Delaroche (KD) nucleon-nucleus optical potential computed at several energies of the projectile.

for the imaginary part and we see that its strength increases when the energy of the projectile grows, due to the fact that at higher energy more inelastic channels are open. On the other hand, the imaginary part computed with the MOPG develops, for both reactions, a very well-marked peak at the surface, which indicates its strong absorptive character at the surface of the target. When the energy of the projectile increases, the volume absorption in the interior of the target is more relevant, as far as the higher energy of the projectile allows exploring the inner part of the target. This volume absorption also increases with the mass of the target and becomes stronger than the surface absorption in the case of heavy ^{208}Pb targets. These trends are also observed in other similar calculations of the optical potential designed for describing the scattering of light particles based on the Skyrme forces [39–42]. It is interesting that the central real and imaginary parts of the phenomenological optical potentials for describing the elastic scattering of ^{2}H [61], ^{3}H and ^{3}He [62], and ^{4}He [63] also show for a given target similar trends as a function of the energy.

As pointed out in our previous work [18], the nucleon-nucleus microscopic optical potential based on the Gogny force predicts more absorption, in particular at high energy of the projectile, but roughly similar real part compared to phenomenological optical potentials, for example Köning-Delaroche (see in this respect Figs. 1 and 2 of [18]). We expect that this behavior of the nucleon-nucleus potential may have a relevant impact on the MOPG owing to Eq. (8). In order to get an improvement of the description of the elastic scattering of light particles by nuclei using the MOPG model, inspired by Ref. [10] we have renormalized the central real and imaginary parts and the spin-orbit term of the Gogny nucleon-nucleus optical potential by energy-dependent factors

TABLE II. Real and imaginary parts of the phenomenological optical potentials (POP) that describe the scattering of ^{2}H [61], ^{3}H and ^{3}He [62], and ^{4}He at the R_{SA} for different reactions at several energies. The predictions of the theoretical models MOPG, RMOPG, and KD at the phenomenological R_{SA} are also given.

E (MeV)	R_{SA} (fm)	V_{POP} (MeV) W_{POP} (MeV)	V_{KD} (MeV) W_{KD} (MeV)	V_{MOPG} (MeV) W_{MOPG} (MeV)	V_{RMOPG} (MeV) W_{RMOPG} (MeV)
			$^{2}\text{H} + {}^{208}\text{Pb}$		
30	10.772	−0.618	−1.625	−1.259	−1.339
		−1.412	−0.732	−0.603	−0.461
70	10.384	−0.856	−2.189	−1.866	−1.809
		−2.321	−1.084	−1.725	−0.967
110	10.240	−0.812	−2.188	−2.087	−1.880
		−2.875	−1.116	−2.266	−1.246
			$^{3}\text{H} + {}^{120}\text{Sn}$		
40	9.536	−1.394	−1.838	−1.266	−1.366
		−1.308	−0.803	−0.785	−0.639
70	9.140	−2.167	−2.924	−2.326	−2.414
		−1.487	−1.386	−2.009	−1.296
100	8.872	−2.876	−3.862	−3.410	−3.433
		−2.279	−1.826	−3.343	−1.827
			$^{3}\text{He} + {}^{40}\text{Ca}$		
20	8.002	−0.848	−1.305	−0.863	−0.972
		−1.001	−0.535	−0.359	−0.359
80	7.040	−2.514	−3.995	−3.841	−3.848
		−2.401	−2.086	−3.493	−2.130
120	6.729	−3.464	−5.252	−5.683	−5.369
		−3.004	−2.642	−5.725	−3.015
			$^{4}\text{He} + {}^{208}\text{Pb}$		
50	10.922	−1.607	−1.958	−1.234	−1.330
		−0.825	−0.965	−0.440	−0.365
150	10.217	−3.040	−4.348	−3.619	−3.459
		−2.478	−2.469	−4.018	−2.223
250	9.959	−2.701	−4.983	−5.056	−4.439
		−3.778	−2.873	−6.193	−3.640

following the protocol discussed in the Appendix. This renormalized MOPG (RMOPG from now on) is also displayed in Fig. 1. The renormalization makes the real part deeper at low bombarding energies and shallower at high energies following, roughly, a smooth transition. As a function of the energy of the projectile, the renormalization reduces strongly the imaginary part at high energy but only a little at low energy. Also, the surface bump is damped by the renormalization. The RMOPG predictions are quite similar to those obtained by using an extended Watanabe potential Eq. (8) built up using the phenomenological nucleon-nucleus optical potential of Köning and Delaroche (KD in the following), as can be seen in Fig. 2 where we display the real and imaginary parts for the $^{3}\text{H} + {}^{120}\text{Sn}$ and $^{3}\text{He} + {}^{40}\text{Ca}$ reactions at several energies computed with both models. For the first reaction the real parts predicted by the RMOPG and KD models are almost identical, while for the second reaction the predictions of these two models differ more, probably due to the smaller mass of the target. Regarding the imaginary central part, the RMOPG and KD models predict a surface bump, which for $^{3}\text{H} + {}^{120}\text{Sn}$ is roughly independent of the energy, whereas for $^{3}\text{He} + {}^{40}\text{Ca}$ it shows an increasing trend with increasing energy of the incident particle, this behavior being more pronounced in the RMOPG case. The imaginary part also contains a volume absorption region, which increases with the growing energy of the projectile and with the mass of the target in both models.

The most relevant part of the optical potential for the nucleus-nucleus elastic scattering is the tail of the potential, in particular at the strong absorption radius R_{SA}, which is closely related to the reaction cross section (see for instance [64] and references therein). In Table II we give the R_{SA} values corresponding to the reactions and energies displayed in Figs. 1 and 2 obtained using the phenomenological optical potentials that describe the elastic scattering of ^{2}H [61], ^{3}H and ^{3}He [62], and ^{4}He [63]. The R_{SA} is defined as the distance of the closest approach of the trajectory with angular momentum L corresponding to transparency function $|S_L| = 0.5$, which in the low energy regime, such as the one considered in this work, can be approximated by the closest distance reached by the Coulomb orbit with $|S_L| = 0.5$. Notice that the R_{SA} extracted with the theoretical models used in this work, namely KD, MOPG, and RMOPG, provide values very close to the ones reported in this table. For the sake of clarity, we will use the R_{SA} obtained from the phenomenological optical potential in what follows. In the same table, we also show the values of the real and imaginary parts of the central term of the optical potential at R_{SA} computed with the aforementioned phenomenological optical potential and with the different theoretical models discussed in this work. From this table, we can see that the values of the real and imaginary parts at the $R_{\rm SA}$ predicted by the theoretical models, in particular by the KD and RMOPG ones, agree quite well among them. This fact suggests that the scattering observables computed with these models should be quite similar [65]. However, the optical potentials at $R_{\rm SA}$ computed with the theoretical models differ more from the predictions of the phenomenological ones. This implies that the theoretical predictions, obtained with global models, will reproduce the experimental data less accurately than the local phenomenological optical potentials specifically designed for describing a given reaction. However, it should also be noted that the real and imaginary parts of the optical potentials for describing light-particle scattering are quite deep and vary rapidly with the distance. Therefore the differences in Table II could have less impact on the calculation of scattering observables than appears at first sight, as we will see in the next discussions.

B. Angular distributions

We want now to investigate the predictive power of the light-particle–nucleus microscopical optical potential based of the Gogny interaction derived in this work. To get some insight about the dependence of the angular distributions on the mass of the target and the energy of the projectile, we display in Figs. 3–6 the elastic scattering angular distributions in Rutherford units of incident ^{2}H at 56 MeV, ^{3}H at 33 MeV, ^{3}He at 119 MeV, and ^{4}He at 35 and 104 MeV from different targets. Globally, we see from these figures that the MOPG, which does not contain free parameters fitted to scattering data, reproduces the experimental results in a quite satisfactory way.

In the case of elastic scattering of deuterons at 56 MeV on targets from ^{16}O to ^{208}Pb, we see that our renormalized model RMOPG reproduces very nicely the experimental behavior [66] of not only the dips at low scattering angles but also for larger scattering angles. We also see in the upper panel that the unrenormalized model MOPG is also in good agreement with the experiment in the dips but for larger scattering angles predicts a slightly smaller differential cross section than the experimental data and shows a smooth oscillatory trend in disagreement with the experiment. In the lower panel, we compare the RMOPG and KD results. We see that both models show almost an identical behavior reproducing fairly well the experimental data with a few exceptions [66].

The breakup of loosely bound projectiles, such as ^{2}H, ^{3}H, or ^{3}He, has a relevant impact on the elastic scattering of such types of projectiles. For the reasons pointed out before, in the present work we have used the simplest approach proposed in the original paper of Watanabe, which includes the breakup effects as a whole in the imaginary part of the optical potential [44]. However, in order to assess the reliability of our approach, we display in Fig. 4 the differential cross sections obtained with our approach (solid line) and with the CDCC method (dashed line) using in both calculations the KD model. From this figure, we see that the predictions of our approach are reasonable, reproducing quite well the experimental data and with an overall agreement with the CDCC results taken from Ref. [50], which, as expected, reproduce slightly better the experimental values.

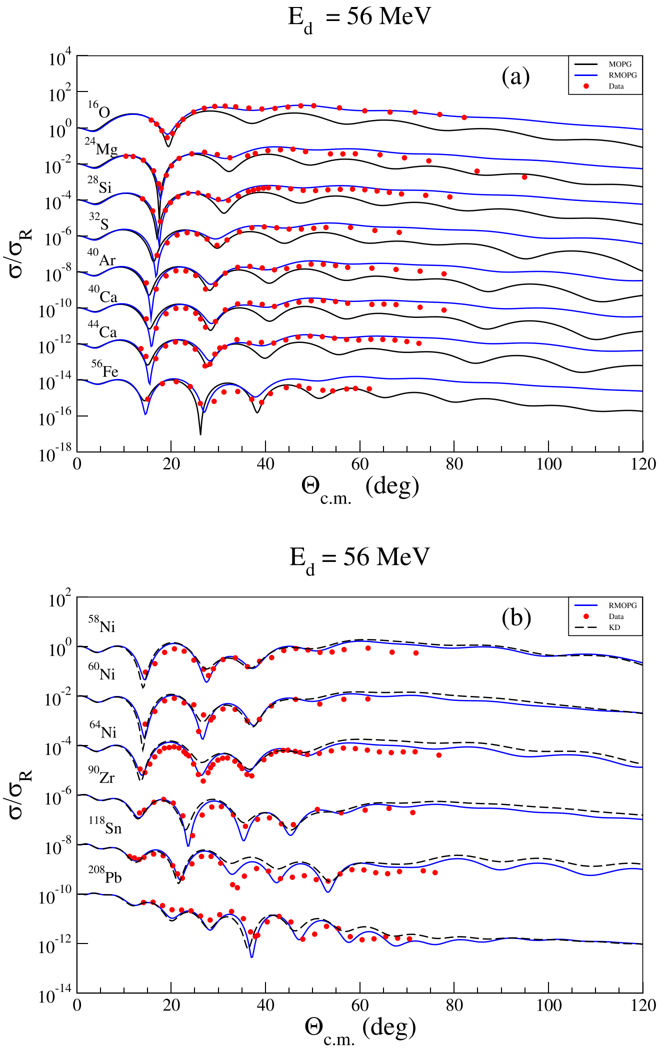

FIG. 3. Angular distributions in Rutherford units of the elastic scattering of deuterons with an incident energy of 56 MeV by several target nuclei from ^{16}O to ^{208}Pb predicted by the RMOPG model compared to the MOPG (a) and KD (b) results. The experimental data are taken from [66]. Note that, except for the topmost one, each angular distribution is offset by a factor of 100 from the preceding one.

In the two panels of Fig. 5, we display the angular distributions of incident ^{3}H and ^{3}He at energies of 33 and 119 MeV, respectively, scattered by several light and medium mass targets from C to Ni. For ^{3}H scattering the MOPG and RMOPG models predict similar results for all the considered reactions [68]. Both models reproduce reasonably well the experimental dips up to a scattering angle of about 50°. Beyond this angle, the experimental behavior is qualitatively reproduced in the case of the ^{12}C, ^{16}O, ^{40}Ca, and ^{48}Ca targets and less so in the case of ^{24}Mg and ^{58}Ni, where a lack of absorption in the two theoretical calculations is observed. The predictions of our model for the scattering of ^{3}He projectiles also reproduce the experimental data [69] at low scattering angles in a reasonable

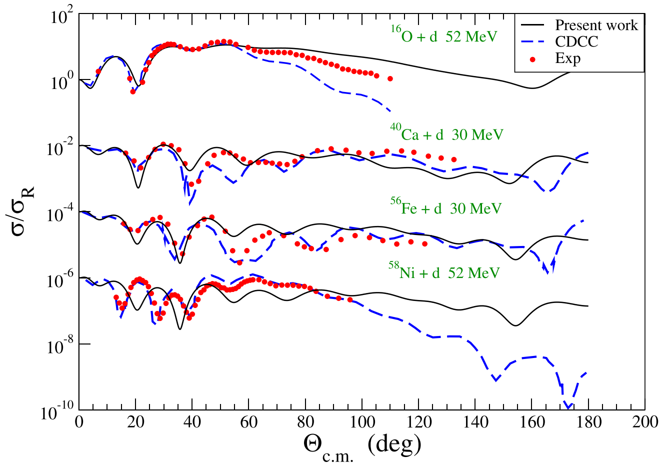

FIG. 4. Angular distributions in Rutherford units of the elastic scattering of deuterons on different targets obtained using the KD model. Solid and dashed lines are the results predicted by the approach used in the present work and by the CDCC of Ref. [50]. Experimental values are taken from the EXFOR database [67]. Note that, except for the topmost one, each angular distribution is offset by a factor of 100 from the preceding one.

way. Again the position of the dips in the angular distributions is predicted quite well by the MOPG and RMOPG models. Also, the experimental behavior is reasonably well averaged by our theoretical calculation up to scattering angles of 40°–50°. From these angles on, the experimental data exhibit a decreasing trend, which is not reproduced by our models. It is interesting to note that the behavior of the differential cross sections for scattering angles larger than ≈50° is not reproduced by the KD either, although it is predicted by the phenomenological potential that describes the elastic scattering of $A = 3$ projectiles by heavier targets [62].

In the upper panel of Fig. 6 we display the angular distributions in Rutherford units corresponding to the elastic scattering of α particles by different target nuclei at a given incident energy of 104 MeV [70–73] computed with the MOPG and RMOPG models. We see that these two theoretical calculations predict quite similar differential cross sections, which describe reasonably well the experimental data except for the ^{208}Pb target, where the dips at scattering angles larger than 40° are not reproduced. In the lower panel of this Fig. 6 we display angular distributions relative to Rutherford scattering of α-particle scattering on different targets of mass number $A \approx 60$ computed with the RMOPG and KD models. Both theoretical calculations predict very similar results, which reproduce rather well the experimental data up to scattering angles of about 90°. From this angle on, the agreement between the theoretical predictions and the experiment slightly deteriorates.

Next, we want to investigate the energy dependence of the differential cross sections for a given target. To this end, we display in Fig. 7 the angular distributions of deuterons scattered by a target of ^{24}Mg in the range of energies between 56 and 72 MeV in the upper panel and between 74 and 90 MeV in the lower panel. In the case of elastic scattering of deuterons in the range between 56 and 72 MeV, the MOPG and RMOPG predict quite well the position and depth of the diffraction minima. For larger scattering angles the experimental data decrease. This trend is well reproduced by the RMOPG model while MOPG shows a wiggly pattern with a value slightly smaller than the experimental data due to the large absorption of this model. In the energy range between 74 and 90 MeV, which is displayed in the lower panel, we see that the KD model reproduces nicely the experimental data with a quality similar to that of the RMOPG in the upper panel. The MOPG predictions, which show the same trends as in the upper panel, reproduce the decreasing behavior of the experimental values only in a qualitative way.

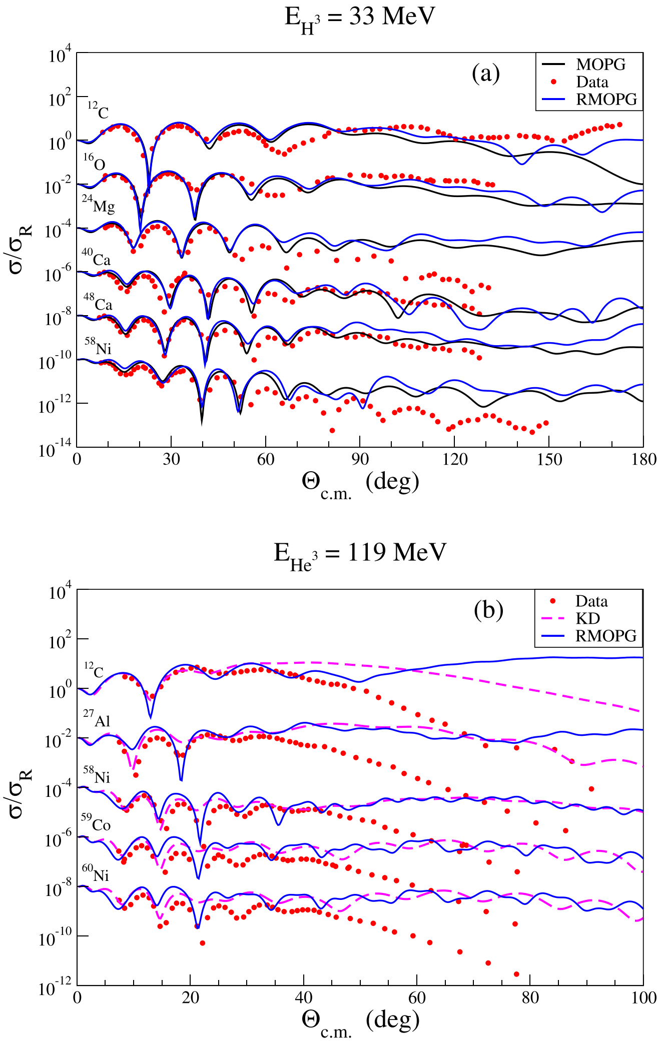

FIG. 5. Angular distributions in Rutherford units of the elastic scattering of ^{3}H with incident energy of 33 MeV from several targets from ^{12}C to ^{58}Ni (a) and of ^{3}He with incident energy of 119 MeV from ^{12}C to ^{60}Ni (b). The experimental data are taken from [68] and [69] for ^{3}H and ^{3}He, respectively. For useful comparisons, we also display the upper (lower) panel the theoretical results computed with the RMOPG and MOPG (RMOPG and KD) models. Note that, except for the topmost one, each angular distribution is offset by a factor of 100 from the preceding one.

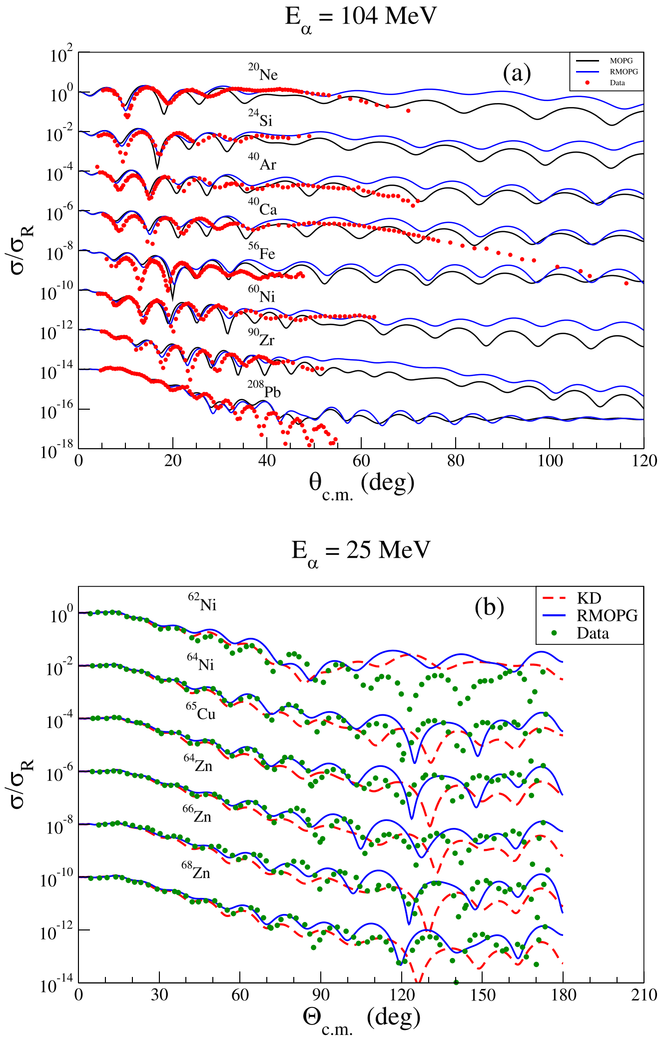

FIG. 6. (a) Angular distributions in Rutherford units of the elastic scattering of α particles with incident energy of 104 MeV by several target nuclei from ^{40}Ca to ^{208}Pb predicted by the MOPG and RMOPG models in comparison with the experimental results [70–73]. (b) Angular distributions in Rutherford units of the elastic scattering of α particles of 25 MeV from several targets of mass number $A \approxeq 60$. The experimental data are taken from [74]. Note that, except for the topmost one, each angular distribution is offset by a factor of 100 from the preceding one.

Although our model is able to describe deuteron, triton, helion, and α-particle scattering by heavier nuclei for scattering angles up to $\approx 40^\circ$–50° in a rather reasonable way, it fails for larger angles where discrepancies with the experimental values can be important. Overall our model is not completely satisfactory due to the following reasons. On the one hand, our global optical potentials for describing light-particle scattering, namely MOPG and RMOPG, are built up with the Watanabe model using the underlying microscopic nucleon-nucleus optical potential derived in Ref. [18]. The former does not contain parameters adjusted to scattering data and the latter has been renormalized using experimental nucleon-nucleus scattering results. Therefore neither of the two models has been fitted to experimental data of light-particle–nucleus scattering, and consequently our models are fully predictive in this respect. Thus it is not surprising that the predictive power of the MOPG and RMOPG is less than that of phenomenological optical models because in the latter case their parameters are fitted to reproduce the scattering data of a given projectile. On the other hand, there are the intrinsic limitations of the folding model, which does not take into account the well-established coupled channels and coupled reaction channels that are very important for an accurate description of the light-particle scattering [46–49]. Calculations including coupling collective states and pickup reactions allow to extract the so-called dynamical polarization potential by inversion of the elastic channel S matrix. This potential added to the folding potential provides a very accurate description of the angular distribution of the elastic cross section [46–49]. In Fig. 8 we display the angular distributions relative to

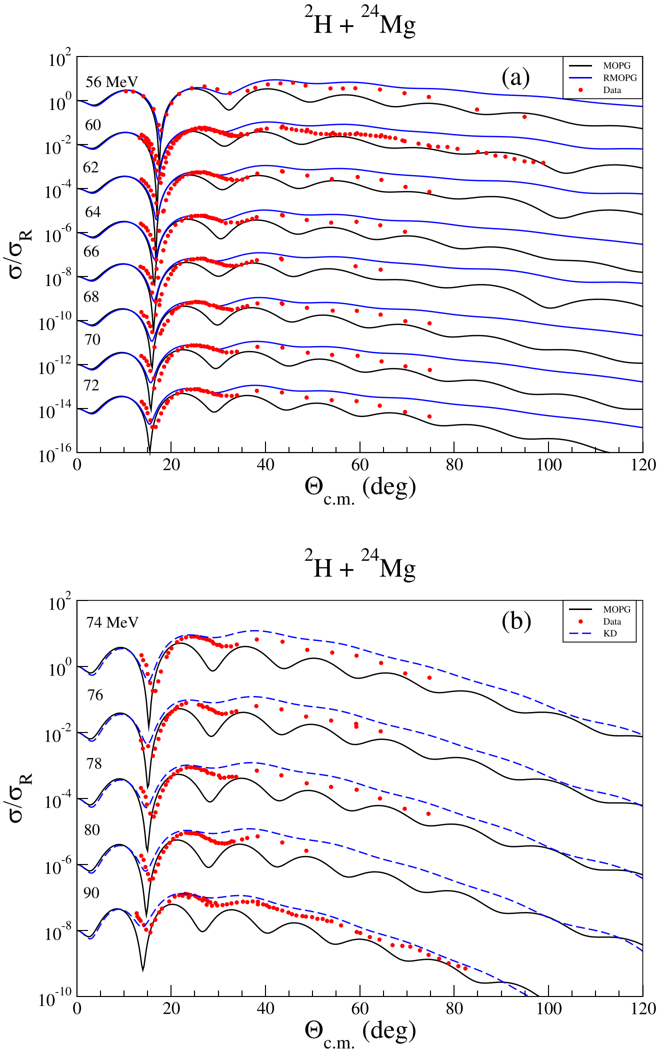

FIG. 7. Angular distributions in Rutherford units of the elastic scattering of deuterons from ^{24}Mg at different incident energies of the projectile computed with the MOPG and RMOPG models (a) and with the MOPG and KD models (b) compared to the experimental values [75,76]. Note that, except for the topmost one, each angular distribution is offset by a factor of 100 from the preceding one.

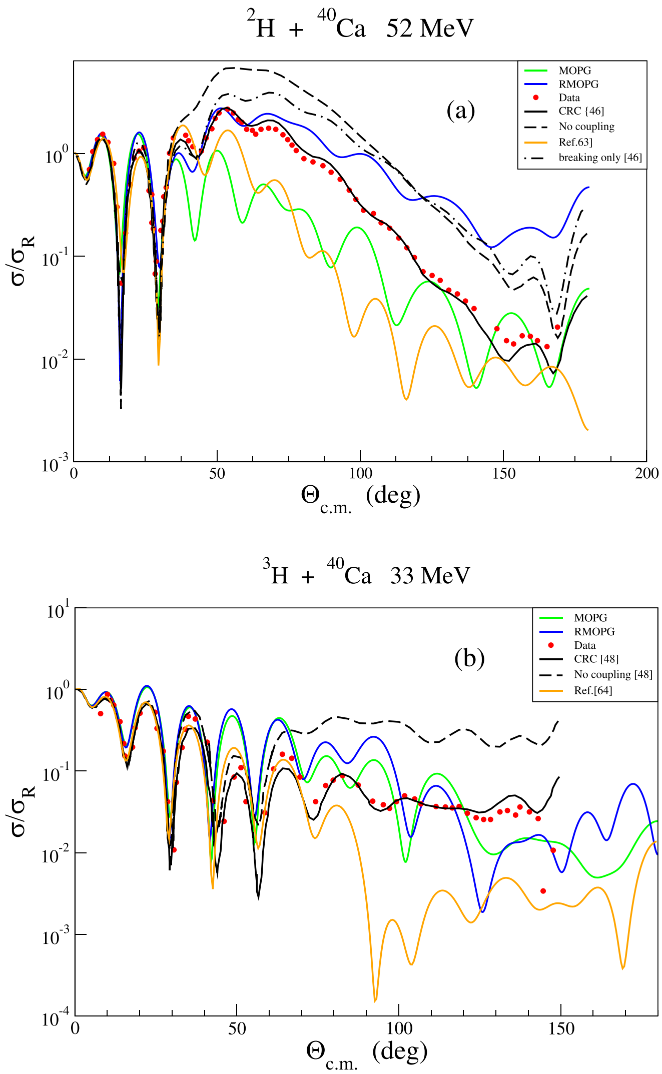

FIG. 8. (a) Angular distributions in Rutherford units of the elastic scattering of deuteron with an incident energy of 52 MeV by a target of ^{40}Ca predicted by the MOPG and RMOPG models in comparison with the results of the CDCC and CRC calculations of Keeley and Mackintosh reported in [46]. The results provided by the phenomenological potential of Ref. [61] are also displayed. (b) The same as in the upper panel for the scattering of triton at 33 MeV by a ^{40}Ca target. The CDCC and CRC results are taken from [48] and the phenomenological predictions from Ref. [62]

TABLE III. Reaction cross sections for ^{2}H-nucleus scattering computed with the MOPG, RMOPG, and KD models computed with the approach used in this work. Some results from the more elaborated CDCC method reported in [50] are also given. Experimental values are taken from Ref. [77]

E (MeV)	Data (mb)	MOPG (mb)	RMOPG (mb)	KD (mb)	CDCC [50]
			^{16}O		
37.9	962 ± 27	1136	1074	1066	1122
65.5	811 ± 19	1067	907	883	943
97.4	726 ± 21	1011	822	745	790
			^{40}Ca		
37.9	1439 ± 43	1568	1503	1487	1590
65.5	1338 ± 28	1556	1391	1361	1424
97.4	1260 ± 30	1486	1274	1175	1244
			^{58}Ni		
37.9	1625 ± 51	1741	1678	1731	1824
65.5	1571 ± 33	1724	1559	1574	1683
97.4	1524 ± 45	1693	1479	1424	1503
			^{120}Sn		
37.9	2240 ± 69	2317	2243	2247	2341
65.5	2346 ± 51	2453	2286	2242	2330
97.4	2351 ± 55	2426	2193	2070	2176
			^{208}Pb		
37.9	2844 ± 142	2643	2576	2676	2736
65.5	3049 ± 71	2976	2809	2865	2937
97.4	3250 ± 82	3043	2797	2781	2881

Rutherford of the ^{2}H + ^{40}Ca at 52 MeV and ^{3}H + ^{40}Ca at 33 MeV reactions computed with the coupled reaction channel method in Refs. [46] and [48], respectively, together with the predictions of our MOPG and RMOPG models. We see that all the folding models displayed in these figure, including the ones of Refs. [46] and [48], describe the experimental data up to scattering angles about 40°–50° and predict very different values for larger angles, which may indicate a failure of the pure folding models. However, when the dynamical polarization potential is added to the folding contribution, the experimental angular distributions are reproduced with very high precision, as can be seen in Fig. 8 and in the results reported in [46–49] and references therein. It is important to point out that the effects of the dynamical polarization potential cannot be recovered by renormalization of the folding potential as discussed in [49]. In Fig. 8 we have also plotted the angular distributions for the above-mentioned reactions computed with the phenomenological optical potentials for deuterons [61] and for tritons [62]. We see that these phenomenological optical potentials describe again the experimental data up to 40°–50° and fail for larger angles, showing that this type of global potentials is not very well suited to deal with scattering on closed-shell targets [47,62].

IV. REACTION CROSS SECTIONS

The reaction cross section measures the flux of incident particles that are removed from the elastic channel because of the nonelastic process. In addition to some technological applications, the main interest of the study of reaction cross sections lies in the fact that they can be very useful in the analysis of angular distributions in elastic scattering in order to eliminate ambiguities of the optical potential [78]. The study of nonelastic reactions requires accurate optical potentials because the imaginary part of their phase shifts determines not only the reaction cross sections but also the amplitude of the partial waves entering in the distorted-wave calculations needed to describe the inelastic process. Also, the reaction cross sections may be an important quantity to give global insight into analyzing the predictive power of different optical models. In this section we compare the theoretical reaction cross sections obtained using the MOPG, RMOPG, and KD models for the scattering of ^{2}H at 38, 65, and 97 MeV, ^{3}He

TABLE IV. Reaction cross sections for ^{3}He-nucleus scattering computed with the MOPG, RMOPG, and KD models. Experimental values are taken from Ref. [78].

E (MeV)	Data (mb)	MOPG (mb)	KD (mb)	RMOPG (mb)
^{16}O				
96.4	975 ± 35	1163	1045	1044
137.8	850 ± 50	1115	908	960
167.3	800 ± 25	1090	844	939
^{40}Ca				
96.4	1360 ± 90	1599	1459	1462
137.8	1280 ± 85	1557	1333	1386
167.3	1225 ± 75	1524	1256	1353
^{58}Ni				
96.4	1690 ± 100	1771	1681	1635
137.8	1570 ± 80	1806	1646	1542
167.3	1470 ± 75	1734	1500	1533
^{120}Sn				
96.4	2285 ± 165	2458	2263	2305
137.8	2230 ± 100	2552	2235	2316
167.3	2180 ± 100	2523	2158	2245
^{208}Pb				
96.4	2765 ± 250	2913	2823	2757
137.8	2850 ± 250	3081	2876	2822
167.3	2820 ± 180	3124	2891	2680

TABLE V. Reaction cross sections for ^{4}He-nucleus scattering computed with the MOPG, RMOPG, and KD models. Experimental values are taken from Ref. [79].

E (MeV)	Data (mb)	MOPG (mb)	KD (mb)	RMOPG (mb)
^{16}O				
117.2	973 ± 62	1162	1076	1058
163.9	895 ± 100	1134	990	986
192.4	850 ± 58	1118	945	955
^{40}Ca				
117.2	1470 ± 60	1614	1512	1494
163.9	1410 ± 120	1579	1463	1360
192.4	1370 ± 70	1599	1393	1389
^{60}Ni				
117.2	1670 ± 85	1832	1774	1711
163.9	1700 ± 160	1850	1713	1659
192.4	1610 ± 90	1828	1649	1609
^{120}Sn				
117.2	2360 ± 150	2472	2342	2334
163.9	2380 ± 250	2516	2285	2308
192.4	2300 ± 170	2550	2276	2267
^{208}Pb				
117.2	2990 ± 180	2972	2940	2829
163.9	2720 ± 250	2987	2915	2664
192.4	3900 ± 190	2989	2871	2507

at 98, 138, and 167 MeV, and ^{4}He at 117.2, 163.9, and 192.4 MeV from a set of targets ranging from ^{16}O to ^{208}Pb with the corresponding experimental values, which are taken from Refs. [77], [78] and [79], respectively.

Our theoretical results are collected in Table III for ^{2}H and Table IV for ^{3}He and Table V for ^{4}He. The experimental values of the reaction cross sections increase when the mass of the target grows. As a function of the energy, the lightest targets show, for all the projectiles, a decreasing tendency with increasing energy. These global trends with the mass of the target and the energy of the projectile are fulfilled rather well by our theoretical calculations. In a more quantitative way, we see that for all the projectiles the MOPG without renormalization overestimates the experimental values, except for reactions of ^{2}H and ^{4}He on ^{208}Pb targets, as a consequence of the large imaginary part in the nucleon-nucleus optical potential [18]. The RMOPG and KD models predict cross sections that are quite similar between them and slightly overcome the experimental values for the lightest targets, in particular for the smallest energies. For medium mass nuclei up to ^{120}Sn, both models describe quite accurately the experimental reaction cross sections while for the heaviest target ^{208}Pb both models underestimate the experimental values by an amount that can be about 25% in the case of scattering of ^{4}He. In the particular case of scattering of ^{2}H, we also collect in Table III the CDCC reaction cross sections reported in Ref. [50], which are also computed using the KD model. The CDCC results exceed the values calculated in this work by about 5%, pointing out that our approach takes into account a large amount of the breakup effects, at least those concerning reaction cross sections. In Fig. 9 we display the reaction cross section of the ^{2}H + ^{58}Ni and ^{2}H + ^{208}Pb reactions as a function of the energy of the projectile computed with all the models used in this work. In the case of ^{58}Ni target, we see that the reaction cross section increases with the energy and reaches a maximum at about $E_d \approxeq 20$ MeV and then decreases. However, for ^{208}Pb, the reaction cross section is an increasing function of the energy, at least in the considered range. We also can see that the CDCC predictions and our results computed in this work almost coincide up to an energy of the projectile E_p about 20 MeV for the ^{58}Ni and about 40 MeV for the ^{208}Pb target. From these energies on, the CDCC prediction is larger by ≈5% than the result computed in this work as a consequence of the better description of the breakup effects. For both reactions and energies below 40–50 MeV, the KD cross sections are larger than the values predicted by the MOPG and RMOPG models, and the opposite trend happens for higher energies. In this region and for the ^{58}Ni target, the MOPG and CDCC results are larger than the experimental data, while the RMOPG and KD results, computed with the extended Watanabe approach used in this work, reproduce quite accurately the experimental values. For the ^{208}Pb target the experimental reaction cross sections are underestimated by all the models considered, the MOPG without renormalization being the model that better agrees with the experimental data.

V. SUMMARY AND CONCLUSIONS

We have derived a microscopic optical potential to describe the elastic scattering of light particles, such as deuterons, tritons, helions, and α particles from heavier target nuclei. This optical potential is obtained through an extended Watanabe model, whose basic ingredients are the neutron-nucleus and proton-nucleus optical potentials and the projectile

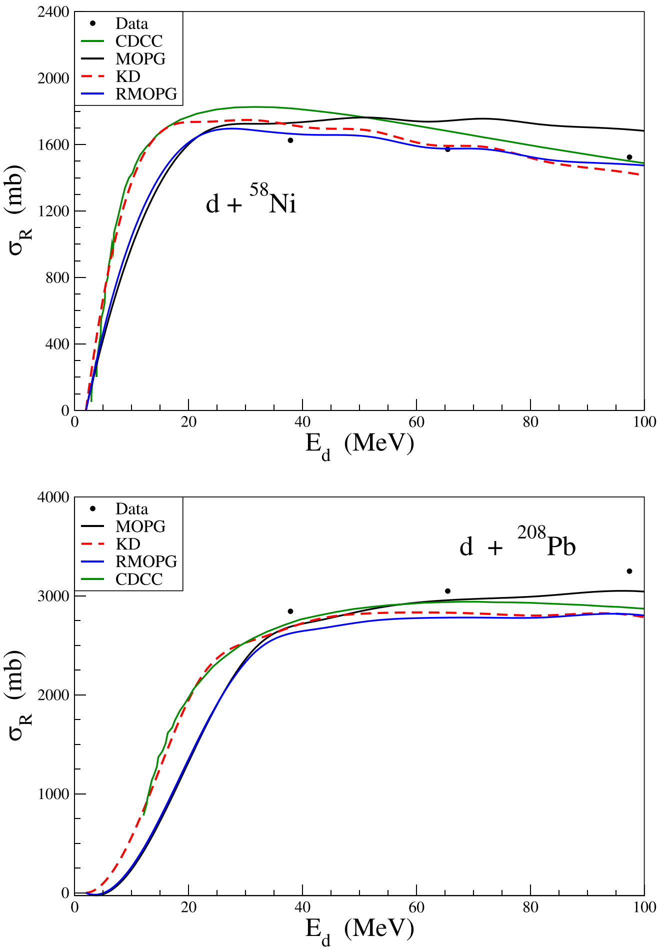

FIG. 9. Reaction cross sections as a function of the energy of the incident deuteron on ^{58}Ni (top) and ^{208}Pb (bottom) computed with the approach developed in this work using the MOPG, RMOPG, and KD models. The predictions of the CDCC method taken from [50] are also displayed.

wave functions. This simple model neglects the interaction among the nucleons of the projectile and assumes that effects from dissociation and distortion of the wave function of the projectile can be included phenomenologically in the imaginary part of the optical potential. Effects due to inelastic and pickup reactions have not been considered either in our simple model. The nucleon-nucleus optical potential used here was derived in a previous work within a semimicroscopic nuclear matter approach where the real and imaginary parts are given, respectively, by the first- and second-order terms of the mass operator, which is determined by means of a Brueckner-Hartree-Fock calculation using a G matrix built up with an effective Gogny interaction. This nucleon-nucleus potential is supplemented by the Coulomb potential for incident protons and by a real spin-orbit potential obtained from a self-consistent quasilocal HF calculation in the target nucleus.

As is expected, for all the projectiles considered, the real and imaginary parts of the theoretical light-particle–nucleus optical potential derived in this work decrease and increase, respectively, when the energy of the projectile grows. At low incident energy, the imaginary part is strongly peaked at the surface. When the energy increases the volume absorption grows and the relative surface absorption diminishes. The angular distribution of the elastic scattering of light particles at different energies from different target nuclei computed with the optical potential derived in this work exhibits reasonably agreement with the experimental data, although the quality depends on the reaction. In general, for scattering angles below 50°, the diffraction pattern of the experimental data at high enough incident energy is quite well reproduced by our calculations, as well as the positions of the first dips. For larger scattering angles there are discrepancies between the values of the differential cross sections predicted by our model and the experimental values, pointing out to a too strong absorption for light targets, although this trend is reversed for heavier nuclei. The cross sections computed with our model decrease with the growing energy of the projectile for light and medium mass targets while the contrary happens for the heaviest target analyzed in this work, namely ^{208}Pb, which is in agreement with the experimental trend. However, the values calculated with our MOPG model for all the targets except ^{208}Pb overestimate the experimental values, especially in the case of the lightest targets with mass numbers smaller than $A = 40$.

To have a better insight into the quality of the results obtained with the MOPG model, we have repeated the theoretical calculations within an extended Watanabe model but using the Köning-Delaroche nucleon-nucleus optical potential instead of the optical potential based on the Gogny interaction. These KD optical potentials for describing the elastic scattering of light particles predict angular distributions and reaction cross sections in better agreement with the experiment than our MOPG model. We have also used this KD model in the case of deuteron scattering to compare our extended Watanabe prescription with the results provided by the more elaborated CDCC method, which takes into account explicitly the breakup effects. We find that the CDCC method improves slightly the angular distributions and provides reaction cross sections about 6–7% larger.

To obtain a better description of light-particle elastic scattering with our model, we improve the starting nucleon-nucleus potential by renormalizing with energy-dependent factors the real and imaginary parts of the central contribution and the spin-orbit potential following the protocol described in the Appendix. This renormalized nucleon-nucleus potential, also based on the Gogny interaction, predicts a description of the nucleon-nucleus elastic scattering quite similar to the one provided by the Köning-Delaroche model in spite of the fact that the fitting procedures of the two models are clearly different. The use of these renormalized nucleon-nucleus potentials in the extended Watanabe approach produces the RMOPG model, which describes light-particle elastic scattering with a quality similar to that obtained with the KD model. In particular, the angular distributions computed with the RMOPG model reproduce the dips at small scattering angles and the exponential falloff at large scattering data in much better agreement with the experiment than the unrenormalized MOPG results. The reaction cross sections computed with the RMOPG are smaller than the ones calculated with the unrenormalized MOPG model and quite similar to the values predicted by the KD model. We have also

TABLE VI. Numerical values of the parameters of the energy-dependent renormalization functions M_α, M_β, and M_γ for proton-nucleus reactions described with the MOPG.

$M_\alpha(E,\lambda_k)=\lambda_1E^2+\lambda_2E+\lambda_3$		
λ_1	λ_2	λ_3
4.555×10^{-5}	-9.5351×10^{-3}	1.1801
$M_\beta(E,\mu_k)=\mu_1E^2+\mu_2E+\mu_3$		
μ_1	μ_2	μ_3
1.0069×10^{-4}	-1.1196×10^{-2}	0.8684
$M_\gamma(E,\delta_k)=\delta_1E^2+\delta_2E+\delta_3$		
δ_1	δ_2	δ_3
-1.0329×10^{-5}	1.7524×10^{-3}	0.6147

checked that the results discussed in this work are compatible with other folding calculations using nucleon-nucleus microscopic optical models built up with the Skyrme interaction.

Overall our Watanabe model based on the Gogny force can provide a qualitative description of the light projectile-nucleus elastic scattering. In particular, the angular distributions up to scattering angles about 40°–50° reproduce the experimental data fairly well but fail for larger angles. Apart from its global character, the lack of accuracy in our model, as well as in any other obtained using the folding method, is due to the absence of inelastic and reaction channels in the elastic scattering calculation. A more accurate description of the systematic of the elastic scattering of light particle by heavier nuclei requires local information about the structure of the target and nearby nuclei, which is the necessary input for dealing with the more sophisticated CDCC and CRC calculations.

Although numerical results obtained with the Gogny models are available from the authors on request, an important and urgent task is to publish the numerical code. Work in this direction is in progress. There is, however, room for improvements of the approach described in this work, for instance implementing CDCC or CRC calculations on top of our Gogny model, including a more accurate description of the Coulomb interaction, or considering explicitly the dipole polarizability in the deuteron scattering around the Coulomb barrier.

ACKNOWLEDGMENTS

Useful discussions with J. N. De and A. Bhagwat are warmly acknowledged. One of the authors (X.V.) acknowledges the partial support from Grants No. PID2020-118758GBI00 and No. CEX2019-000918-M (through the "Unit of Excellence María de Maeztu 2020-2023" award to ICCUB) from the Spanish MCIN/AEI [80].

TABLE VII. Numerical values of the parameters of the energy-dependent renormalization functions M_α, M_β, and M_γ for neutron-nucleus reactions described with the MOPG.

$M_\alpha(E,\lambda_k)=\lambda_1e^{-\lambda_2E}+\lambda_3$			
λ_1	λ_2	λ_3	
0.3019	0.2577	1.0858	
$M_\beta(E,\mu_k)=\dfrac{\mu_1E^2+\mu_2E+\mu_3}{E+\mu_4}$			
μ_1	μ_2	μ_3	μ_4
0.23856	−19.3728	575.8818	383.7557
$M_\gamma(E,\delta_k)=\delta_1e^{\delta_2E}+\delta_3$			
δ_1	δ_2	δ_3	
4.4806×10^{-2}	0.1	0.5466	

APPENDIX

As pointed out in the main text, the imaginary part of MOPG for light particles is too strong compared to the predictions of the KD model and the phenomenological models fitted to describe the elastic scattering of this kind of particles [61–63]. This fact is, actually, a direct consequence of the strong absorption in the nucleon-nucleus Gogny model, as pointed out in [18]. To cure this unwanted effect, we renormalize with energy-dependent factors the real and imaginary parts of the central term of the nucleon-nucleus Gogny potential as well as its corresponding spin-orbit contribution, in a similar way as was done in Ref. [10] with the Jeukene, Lejeune, and Mahaux optical potential.

To this end we first select a set of 45 proton-nucleus and 22 neutron-nucleus reactions on targets of ^{40}Ca, ^{56}Fe, ^{90}Zr, ^{120}Sn, and ^{208}Pb for which experimental angular distributions of elastic scattering in the energy ranges between 10 and 100 MeV (for protons) and between 5 and 26 MeV (for neutrons) exist in the EXFOR database [67]. Next, for each reaction and each energy, we determine the coefficients α, β, and γ, which multiply the real central part, the imaginary central part, and the spin-orbit contribution of the Gogny optical potential, in such a way that the renormalized potential minimizes the relative rms buildup as

$$\mathrm{rms}^2=\frac{1}{N_1}\sum_{i=1}^{N}\left[\frac{\sigma_{\mathrm{exp}_i}-\sigma_{\mathrm{th}}(\alpha,\beta,\gamma)_i}{\sigma_{\mathrm{exp}_i}}\right]^2, \tag{A1}$$

where σ_{exp_i} are the N_1 experimental values of the differential cross section for each considered reaction taken from [67] and σ_{th} the corresponding theoretical values computed with the renormalized potential. We fit these two set of 45 (protons) and 22 (neutrons) of $\{(\alpha,\beta,\gamma)\}$ pseudodata by suitable analytical functions, which allow determining the energy-dependent factors that have to be used to renormalize the Gogny optical potential for any nucleon-nucleus reaction. To this end, we chose the renormalization functions $M_\alpha(E,\lambda_k)$, $M_\beta(E,\mu_k)$ and $M_\gamma(E,\delta_k)$ given in Table VI for protons and in Table VII for neutrons. These functions depend on the energy of the projectile and on 3–4 parameters, which are determined by minimizing the relative rms between each set of pseudodata and corresponding fitting functions. For example, for the set of pseudodata $\{\alpha_i\}$ and the fitting function $M_\alpha(E,\lambda_k)$, we obtain the λ_1, λ_2, and λ_3 parameters by minimizing

$$\mathrm{rms}^2=\frac{1}{N_2}\sum_{i=1}^{N}\left[\frac{\alpha_i-M_\alpha(E_i,\lambda_k)}{\alpha_i}\right]^2, \tag{A2}$$

where now the sum runs over the considered proton-nucleus (neutron-nucleus) reactions, N_2 being the total number of reactions, i.e., 45 for protons and 22 for neutrons.

[1] P. E. Hodgson, *The Optical Model of Elastic Scattering* (Clarendon, Oxford, 1963).
[2] F. D. Becchetti and G. W. Greenlees, Phys. Rev. **182**, 1190 (1969).
[3] R. L. Varner, W. J. Thomson, T. L. Abbe, E. J. Ludwig, and T. B. Clegg, Phys. Rep. **201**, 57 (1991).
[4] A. J. Koning and J. P. Delaroche, Nucl. Phys. A **713**, 231 (2003).
[5] J. S. Bell and E. J. Squires, Phys. Rev. Lett. **3**, 96 (1959).
[6] J. P. Jeukenne, A. Lejeune, and C. Mahaux, Phys. Rev. C **10**, 1391 (1974).
[7] J. P. Jeukenne, A. Lejeune, and C. Mahaux, Phys. Rep. **25**, 83 (1976).
[8] J. P. Jeukenne, A. Lejeune, and C. Mahaux, Phys. Rev. C **15**, 10 (1977).
[9] J. P. Jeukenne, A. Lejeune, and C. Mahaux, Phys. Rev. C **16**, 80 (1977).
[10] E. Bauge, J. P. Delaroche, and M. Girod, Phys. Rev. C **58**, 1118 (1998).
[11] D. Vautherin and D. M. Brink, Phys. Rev. C **5**, 626 (1972).
[12] J. Dechargé and D. Gogny, Phys. Rev. C **21**, 1568 (1980).
[13] S. Qingbiao, Z. Jingshang, T. Ye, M. Zhongyu, and Z. Yizhong, Z. Phys. A **303**, 69 (1981).
[14] Q.-B. Shen, Y.-L. Han, and H.-R. Guo, Phys. Rev. C **80**, 024604 (2009).
[15] Y.-L. Xu, H.-R. Guo, Y.-L. Han, and Q.-B. Shen, J. Phys. G: Nucl. Part. Phys. **41**, 015101 (2014).
[16] V. V. Pilipenko, V. I. Kuprikov, and A. P. Soznik, Phys. Rev. C **81**, 044614 (2010).
[17] V. V. Pilipenko and V. I. Kuprikov, Phys. Rev. C **86**, 064613 (2012).
[18] J. Lopez-Moraña and X. Viñas, J. Phys. G: Nucl. Part. Phys. **48**, 035104 (2021).
[19] B. Sinha, Phys. Rep. **20**, 1 (1975).
[20] F. A. Brieva and J. R. Rook, Nucl. Phys. A **291**, 299 (1977); **291**, 317 (1977); **297**, 206 (1978).
[21] H. F. Arellano, F. A. Brieva, and W. G. Love, Phys. Rev. C **41**, 2188 (1990); **50**, 2480 (1994); **52**, 301 (1995).
[22] H. F. Arellano and E. Bauge, Phys. Rev. C **76**, 014613 (2007); H. F. Arellano, F. A. Brieva, and W. G. Love, *ibid.* **84**, 034606 (2011).
[23] F. J. Aguayo and H. F. Arellano, Phys. Rev. C **78**, 014608 (2008).
[24] K. Amos, P. J. Dortmans, H. V. von Geramb, S. Karataglidis, and J. Raynnal, Adv. Nucl. Phys. **25**, 276 (2000).
[25] D. T. Khoa, E. Khan, G. Colò, and N. Van Giai, Nucl. Phys. A **706**, 61 (2002).
[26] D. T. Loan, D. T. Khoa, and N. H. Phuc, J. Phys. G: Nucl. Part. Phys. **47**, 035106 (2020).
[27] K. Egashira, K. Minomo, M. Toyokawa, T. Matsumoto, and M. Yahiro, Phys. Rev. C **89**, 064611 (2014).
[28] H. Feshbach, *Theoretical Nuclear Physics* (Wiley, New York, 1992), Vol. II.
[29] G. R. Satchler, *Direct Nuclear Reactions* (Clarendon, Oxford, 1983).
[30] G. R. Satchler and W. G. Love, Phys. Rep. **55**, 183 (1979).
[31] M. E. Brandan and G. R. Satchler, Phys. Rep. **285**, 143 (1997).
[32] X. Li, H. An, and C. Cai, Eur. Phys. J. A **39**, 255 (2009).
[33] D. Y. Pang, Y. L. Ye, and F. R. Xu, Phys. Rev. C **83**, 064619 (2011).
[34] V. B. Soubbotin and X. Viñas, Nucl. Phys. A **665**, 291 (2000)
[35] V. B. Soubbotin, V. I. Tselyaev, and X. Viñas, Phys. Rev. C **67**, 014324 (2003).
[36] J. Lopez Moraña and X. Viñas, J. Phys. G: Nucl. Part. Phys. **50**, 045108 (2023).
[37] V. V. Pilipenko and V. I. Kuprikov, Phys. Rev. C **92**, 014616 (2015).
[38] V. I. Kuprikov, V. V. Pilipenko, and A. P. Soznik, Phys. Atom. Nuclei **75**, 832 (2012).
[39] H.-R. Guo, Y.-L. Xu, Y.-L. Han, and Q.-B. Shen, Phys. Rev. C **81**, 044617 (2010).
[40] H.-R. Guo, Y.-L. Xu, Y.-L. Han, and Q.-B. Shen, Nucl. Phys. A **922**, 84 (2014).
[41] H.-R. Guo, Y. Zhang, Y.-L. Han, and Q.-B. Shen, Phys. Rev. C **79**, 064601 (2009).
[42] H.-R. Guo, Y.-L. Xu, H.-Y. Liang, Y.-L. Han, and Q.-B. Shen, Phys. Rev. C **83**, 064618 (2011).
[43] V. I. Kuprikov and V. V. Pilipenko, Phys. Rev. C **94**, 064612 (2016).
[44] S. Watanabe, Nucl. Phys. **8**, 484 (1958).
[45] G. H. Rawitscher, Phys. Rev. C **9**, 2210 (1974).
[46] N. Keeley and R. S. Mackintosh, Phys. Rev. C **77**, 054603 (2008).
[47] R. S. Mackintosh and N. Keeley, Phys. Rev. C **100**, 064613 (2019).
[48] N. Keeley and R. S. Mackintosh, Phys. Rev. C **102**, 064611 (2020).
[49] N. Keeley and R. S. Mackintosh, Phys. Rev. C **107**, 034602 (2023).
[50] P. Chau Huu-Tai, Nucl. Phys. A **773**, 56 (2006).
[51] M. V. Andrés, J. Gómez-Camacho, and M. A. Nagarajan, Nucl. Phys. A **579**, 273 (1994).
[52] A. M. Moro and J. Gómez-Camacho, Nucl. Phys. A **648**, 141 (1999).
[53] N. Austern, Y. Iseri, M. Kamimura, M. Kawai, G. Rawitscher, and M. Yahiro, Phys. Rep. **154**, 125 (1987).
[54] J. F. Berger, M. Girod, and D. Gogny, Comput. Phys. Commun. **63**, 365 (1991).
[55] CEA web page, https://www-phynu.cea.fr.
[56] N. Pillet and S. Hilaire, Eur. Phys. J. A **53**, 193 (2017).
[57] F. Chappert, M. Girod, and S. Hilaire, Phys. Lett. B **668**, 420 (2008).
[58] S. Goriely, S. Hilaire, M. Girod, and S. Peru, Phys. Rev. Lett. **102**, 242501 (2009).
[59] J. Lei and A. M. Moro, Phys. Rev. Lett. **122**, 042503 (2019).
[60] G. Baur, Phys. Lett. B **178**, 135 (1986).
[61] Y. Han, Y. Shi, and Q. Shen, Phys. Rev. C **74**, 044615 (2006).
[62] D. Y. Pang, P. Roussel-Chomaz, H. Savajols, R. L. Varner, and R. Wolski, Phys. Rev. C **79**, 024615 (2009).
[63] X.-W. Su and Y.-L. Han, Int. J. Mod. Phys. E **24**, 1550092 (2015).
[64] A. Bhagwat and Y. K. Gambhir, J. Phys. G: Nucl. Part. Phys. **36**, 025105 (2009).
[65] D. Roubos, A. Pakou, N. Alamanos, and K. Rusek, Phys. Rev. C **73**, 051603(R) (2006).
[66] K. Hatanaka, K. Imai, S. Kobayashi, T. Matsusue, M. Nakamura, K. Nisimura, T. Noro, H. Sakamoto, H. Shimizu, and J. Shirai, Nucl. Phys. A **340**, 93 (1980).
[67] Experimental Nuclear Reaction Data (EXFOR) Ddatabase version of 2023-02-13.

[68] J. B. A. England *et al.*, Nucl. Phys. A **475**, 422 (1987).

[69] M. Hyakutake *et al.*, Nucl. Phys. A **311**, 161 (1978).

[70] G. Hauser, R. Löhken, H. Rebel, G. Schatz, G. W. Schweimer, and J. Speth, Nucl. Phys. A **128**, 81 (1969).

[71] H. Rebel, G. W. Schweimer, G. Schatz, J. Speth, R. Löhken, G. Hauser, D. Habs, and H. Klewe-Nebenius, Nucl. Phys. A **182**, 145 (1972).

[72] K. Rebel, R. Löhken, G. W. Schweimer, G. Schatz, and G. Hauser, Z. Phys. **256**, 258 (1972).

[73] H. J. Gils, H. Rebel, G. Nowicki, A. Ciocamel, D. Hartmann, H. Klewe-Nebenius, and H. Wisshak, J. Phys. G **1**, 344 (1975).

[74] J. B. A. England *et al.*, Nucl. Phys. A **388**, 573 (1982).

[75] A. Kiss, O. Aspelund, G. Hrehuss, K. T. Knöfle, M. Rogge, U. Schwinn, Z. Seres, P. Turek, and C. Mayer-Boricke, Nucl. Phys. A **262**, 1 (1976).

[76] C. Bäumer, R. Bassini, A. M. van den Berg, D. De Frenne, D. Frekers, M. Hagemann, V. M. Hannen, M. N. Harakeh, J. Heyse, M. A. de Huu, E. Jacobs, M. Mielke, S. Rakers, R. Schmidt, H. Sohlbach, and H. J. Wörtche, Phys. Rev. C **63**, 037601 (2001).

[77] A. Auce, R. F. Carlson, A. J. Cox, A. Ingemarsson, R. Johansson, P. U. Renberg, O. Sundberg, and G. Tibell, Phys. Rev. C **53**, 2919 (1996).

[78] A. Ingemarsson, G. J. Arendse, A. Auce, R. F. Carlson, A. A. Cowley, A. J. Cox, S. V. Förtsch, R. Johansson, B. R. Karlson, M. Lantz, J. Peavy, J. A. Stander, G. F. Steyn, and G. Tibell, Nucl. Phys. A **696**, 3 (2001).

[79] A. Ingemarsson, J. Nyberg, P. U. Renberg, O. Sundberg, R. F. Carlson, A. J. Cox, A. Auce, R. Johansson, and G. Tibell, D. T. Khoa, and R. E. Warner, Nucl. Phys. A **676**, 3 (2000).

[80] doi: 10.13039/501100011033.